

DOI: 10.1002/ ((please add manuscript number))

Article type: Communication

Reconfiguration of Solar Fuel Ultrathin Films via Periodically Micro-bending for Efficient Photo-electrochemical Water Splitting

Lichao Jia(a), Hongqiang Wang(b)*, Peter Bogdanoff(c), Martina Schmid(d), Ulrike Bloeck(e), and Sebastian Fiechter(c)*

Prof. L. C. Jia

Key Laboratory of Applied Surface and Colloid Chemistry, National Ministry of Education, School of Materials Science and Engineering, Shaanxi Normal University, 620 West Chang'an Street, Xi'an, Shaanxi 710119, China

E-mail: lichaojia@snnu.edu.cn

Prof. H. Q. Wang

State Key Laboratory of Solidification Processing, Center for Nano Energy Materials, School of Materials Science and Engineering, Shaanxi Joint Laboratory of Graphene, Northwestern Polytechnical University, Xi'an, 710072, P. R. China

E-mail: hongqiang.wang@nwpu.edu.cn

Dr. P. Bogdanoff, Prof. S. Fiechter

Institute for Solar Fuels, Helmholtz-Zentrum Berlin für Materialien und Energie GmbH, Hahn-Meitner-Platz 1, 14109 Berlin, Germany

Prof. M. Schmid

Institute Experimental Physics, University of Duisburg, Bismarckstr. 81, 47057 Duisburg, Germany

Miss U. Bloeck,

Department Nanoscale Structures and Microscopic Analysis, Helmholtz-Zentrum Berlin für Materialien und Energie GmbH, Hahn-Meitner-Platz 1, 14109 Berlin, Germany

Keywords: Solar Fuels, Ultrathin Films, Water Splitting, Optical Management, α -Fe₂O₃

Tackling the conflict between the electronic and optical properties of the ultrathin photo-electrode films, is of utmost importance for the development of efficient light-driven electrolyzers. We show in this report an efficient strategy of geometry reconfiguration to design ultrathin photoelectrodes that compensate intrinsic low absorption coefficients and limited charge carrier transport properties. Exemplified by α -Fe₂O₃, this film structure is able to generate an approximately 4.5 fold increase in photocurrent at a bias of 1.23 V versus RHE under simulated solar radiation conditions compared to that of a flat film. The periodically micro-bending of the deposited ultrathin film not only leads to higher light absorbing volume per unit area, but also to complex enhanced light coupling by photonic effects. The 3D

numerical simulations of optical properties of the micro-bent films indicates clearly superior absorption compared to the planar Fe_2O_3 film, and the hemisphere diameter greatly influences the PEC water splitting performance, which are in good agreement with the experimental results. Our results indicate that periodically micro-bending of ultrathin solar fuel films is promising to develop high performance photoelectrodes for light-driven water splitting.

PEC water splitting offers an important strategy to convert solar energy into chemical one that can either immediately be used as a fuel or stored for times when no solar light is available. Enormous time and resources have been invested on developing applicable semiconductor photoelectrodes, which have to feature low cost, abundant constituents, high light absorption, suitable electronic band structures as well as pronounced chemical stability and catalytic activity.^[1] Efficient light harvesting^[2] and charge carrier collection^[3] are the two critical issues that has to be considered in manufacturing cheap, chemically stable and efficient photoelectrodes. Engineering photoelectrode materials into nanostructures^[4] could effectively reduce the electron-hole recombination rates owing to the short charge-carrier diffusion lengths L_D in semiconducting oxide species, whereas a short carrier diffusion length limits the light absorption capability in general^[5]. Enhanced light harvesting by developing complex architectures in the film volume, such as hierarchical^[6, 7] and inverse opal structures^[8-10], which generally increases the light absorption depth, however demands an additional remediation, such as co-catalyst modification^[11] and/or addition of charge transport materials^[12,13] to reduce charge carrier recombination in these skeletons. It is thus challenging to develop ultrathin PEC photoelectrodes that combine both electronic and optical superiorities. One of the recent research endeavors has been directing to the construction of high performance PEC photoelectrodes through optical engineering of ultrathin solar fuel films that intrinsically favors short charge carrier diffusion lengths to facile decouple charge carrier transport and optical absorption.^[14-20] Plasmonic nanostructures on ultrathin films have been

shown to be capable of enhancing the solar energy collection via photonic or/and plasmonic energy transfer enhancement.^[15-17, 21] Internal photonic management of the photoelectrode film via resonant light trapping provides another effective option to improve the PEC water splitting performance.^[14, 19-20] While adopting exotic plasmonic/reflection layers or managing resonant light trapping of the film internally have displayed preliminary success, seeking ways of addressing the trade-off between light absorption and charge carrier collection of solar fuel ultrathin films is still a highly desirable challenge. We present herein an alternative light harvesting amplification via geometrical reconfiguration of the ultrathin films, which supplements the ultrathin film ordered micro-spaces for flexible external photonic management. Exemplified by α -Fe₂O₃, which typically has a short charge carrier diffusion length (2 – 20 nm)^[22,23], the reconfiguration is verified to be able to generate approximately a 4.5 fold increase in photocurrent at a bias of 1.23 V versus RHE under simulated solar radiation.

Scheme 1 depicts how a planar ultrathin film is reconfigured to have supplementary micro-spaces for optical management. A monolayer of polystyrene spheres (PSs) first self-assembles on a desired substrate such as fluorine-doped tin oxide (FTO).^[24] Nitrogen plasma etching process is subsequently adopted to reduce the nanospheres diameter, and the space between two adjacent spheres which can be deliberately tailored via the plasma etching process. Then a desired semiconductor film is deposited via magnetron sputtering on the plasma treated PS/FTO substrate, which is then subjected to calcination to remove the PS templates, leaving behind a film of periodically arrayed hollow hemispheres. A straightforward perception if comparing a deposited planar film with the one composing of the ordered micro-spaces is that the ultrathin planar film is periodically micro-bent. Such photoelectrode with ordered micro-spaces are anticipated to be photosensitive and flexible for photonic management while it keeps the ultrathin film feature. We have thus chosen α -Fe₂O₃ as an example in the present

study to explore the viability of such reconfiguration for improved PEC water splitting. In addition, the versatility of the present strategy combining self-assembly and magnetron sputtering allows for acquiring photosensitive ultrathin films with variable compositions and diameters of defined distances between two adjacent spheres for tunable PEC water splitting.

Figures 1a and **1b** display the typical SEM and TEM cross section images of a film with planar configuration deposited via magnetron sputtering on a fluorine-doped tin oxide (FTO) conductive layer, yielding a flat homogeneous layer of α -Fe₂O₃ with a thickness of around 65 nm. In contrast, after reconfiguration, the periodical micro-bent (see also Figure 1c and d) film consisting of the well-ordered microspheres array is obtained, characterized by a lateral hexagonally close-packed structure over large distances (Figure S1a). In our example the single microsphere size is around 470 nm, which is slightly smaller than the size of a single PS sphere. Closer examination by electron microscopy reveals that the hematite nanospheres are also connected to each other in the space between adjacent spheres, forming a continuous Fe₂O₃ coating on the structured substrate (see Figure S1b). The cross section SEM image shown in Figure 1c indicates that the coating consists of a monolayer of PS spheres and the arrays sub-unit is actually hemispherical. The hollow hemisphere structure with a shell thickness of around 65 nm can be seen in the cross section TEM image shown in Figure 1d, which appears as a periodically micro-bent film connected to the FTO substrate.

It is of fundamental importance to study how the reconfiguration via micro-bending affects the microstructures of the deposited films. The enlarged TEM image (Figure 1e) of a flat film presents the typical single layer columnar grain structure with grain sizes ranging from 50 to 60 nm, vertically deposited on the larger crystal facets of the FTO grains. An enlarged top view of the periodical array of hemispheres (Figure 1f) reveals that each hemisphere is actually composed of particulate crystal grains, forming a micro-arch. Detailed TEM observation (Figure 1g) shows that the deposition on the PS spheres influence the formation of the grain structures because the axes of grains in the bent structure are pointing toward the

center of the hollow spheres. The trapezoidal crystal grains are single crystalline (Figure S1c) and are forming archs on the later removed PS spheres via calcination, which indicates the good affinity in-between the adjacent crystal grains.

X-ray diffraction was employed to investigate the crystallinity and the grain orientation in flat and micro-bent films. For both films, except those peaks belonging to the FTO substrate, all diffraction lines can be assigned to rhombohedral hematite (JCPDS No. 89-0597, Figure 1h). The enhanced intensity of the 104–peak evidences the preferential orientation of grains in the micro-sphere array film architecture (Figure S2), since the orientation of the grains is no longer depending on the arbitrary orientation of the grains of the FTO substrate but by the adjustment of micro-arch forming crystallites. It is worth to note that this periodically micro-bent films can be obtained on various substrates, such as silicon wafers, normal glass and even on curved ceramic tubes, and can be easily peeled off (Figure 1i), indicating its flexibility of being transferred to a desired substrate for different applications in solar fuel and other solar energy devices, as well as optical sensors.

It is visually apparent that strategy of periodically micro-bending generates supplementary spaces that allows interference of the incident light and thus possibility of light management. UV-vis spectroscopy (**Figure 2a**) has been employed to study its light absorption as a function of hemisphere diameter and hemisphere distance as well as a function of incident light angle, to explore if these periodically ordered hollow hemispheres could improve the light trapping ability of the ultrathin film. An intrinsic hematite absorption edge at approximately 600 nm is expected and also visible in Figure 2a for the planar film, indicating a band gap of about 2.06 eV, which is consistent with the results reported by other researchers.^[25,26] Once the hematite ultrathin film was periodically micro-bent, the optical absorption across the entire spectral range is increased, which can be explained by an increased volume of the oxide related to the substrate area owing to the hemisphere microstructure. In addition the incident light can be absorbed in the hollow hemispheres

structured film by coupled optical phenomena, resulting in increased photon absorptions, which does not happen in the case of a planar film (Figure 2e). Therefore, a significant increase in absorption arises compared with the flat film (Figure 2a). In addition a new absorption structure arises with a peak position at 630 nm where the planar film shows total transparency.

The elevated light harvesting via micro-bending for solar fuels generation is further verified via photoelectrochemical measurements performed by a three electrode cell configuration. The planar and micro-bent films deposited on FTO, respectively, were used as working electrodes, a platinum wire served as counter, and a Hg/HgO as reference electrode. The photocurrent densities of both types of films are presented in Figure 2b. It can be clearly seen that the micro-bent film shows a significant photocurrent enhancement in contrast to that of a planar film. The photocurrent intensity rises to 0.59 mA cm^{-2} at 1.23 V vs. RHE , which is about 4.5 times the value of a planar film (0.13 mA cm^{-2}). Upon further potential increase, it can ramp up to 2.4 mA cm^{-2} at $\sim 1.7 \text{ V}$ before the onset of the dark current occurs. Compared with a planar hematite film, the micro-bent film displays a 3-5 times higher photocurrent intensity over the entire potential range from 1.1 to $1.7 \text{ V}_{\text{RHE}}$. These measurements demonstrate that the film with ordered micro-spheres is more efficient in the process of the oxygen evolution reaction (OER) than that of a planar film with respect to photo-energy conversion.

To gain a qualitative understanding of the superiority of the film with ordered micro-spaces to the planar film, both film electrodes were subjected to chronoamperometric measurements using chopped light (current density vs. time at a fixed applied bias potential of $1.3 \text{ V}_{\text{RHE}}$) (Figure 2c). The observed current density peak after switching on the light is proportional to the number of generated charge carriers multiplied by the separation probability of the light excited electron-hole pairs. ^[27, 28] The separation probability indicates how efficient the charge separation in the space charge region is. Here the micro-bent film shows a significantly

higher value although the electrons have to pass longer distances to the point contacts of the micro-arches than the holes which can react with the electrolyte (Figure 1d and 1g). Obviously the transport of electrons migrating along oriented grains in the arches of the hollow hemispheres (see Figure 1g and Figure S1c) to the back contact is here more efficient than in case of a flat film. The observed effect is clearly caused by the improved coupling of light in the present micro-bent structure.

The transient observed in the current density curves indicates the ratio between surface recombination and OER rate at the semiconductor-electrolyte interface (SEI). Under steady state conditions the equilibrium between OER and surface recombination rate is achieved. In the micro-bent film the OER rate is improved compared to the flat film due to a lower surface recombination rate because the transient decay time is not as pronounced as in the case of the micro-bent film. The transient decay time can be calculated from a logarithmic plot of parameter D . D is defined as

$$D = (I_t - I_s) / (I_m - I_s) \quad (1)$$

in which I_t is the photocurrent at time t , I_s is the steady state photocurrent and I_m represents the current density at the photocurrent spike. The transient decay time^[29, 30] is defined as the time at which

$$\ln D = -1 \quad (2)$$

Accordingly, the transient decay time of these two photoanodes are given in Figure 2d. The transit decay time is estimated to be 10.7 s for the micro-bent film, which is two and half times longer than that of the planar film (4.2s), owing to a suppressed charge recombination in the micro-bent film. Owing to the special structure of micro-structured film, the incident light can be multiply scattered within the film and reduce the reflection losses (as shown in Figure 2e). Coupled optical phenomena have also to be considered since the wavelength of the finally absorbed light is larger than the diameter of the hollow hemispheres. Therefore, the

incident light intensity is enhanced to some extent if comparing to the planar film. As reported by Li et al.,^[15] the lifetime of the charge carries could be increased by an increase in the irradiation intensity for hematite, implying that the supplementary micro-spheres could be the reason why the micro-bent film has a lower charge recombination rate. On the other hand it has to be taken into account that electrons, which have to pass a large number of hematite grain boundaries after light excitation migrating from a crystallite in a micro-arch to the FTO back contact, have obviously a less recombination probability.

To further shed light on the PEC enhancement, incident photon-to-electron conversion efficiency (IPCE) spectra were investigated (Figure 2f). The micro-bent hematite film shows a substantially enhanced IPCE over the whole wavelength range from 400 to 700 nm when compared with the planar film, which is consistent with the I–V measurements shown in Figure 2b. The IPCE at 400 nm is 36.8 % and 8.2 % for the hematite micro-bent photoanode and the planar film, respectively. The enhancement at 630 nm is around 20 times larger and this property correlates well with the optical absorption shown in Figure 2a, which further verifies the improved photon capturing capability of the micro-bent film.

The micro-sphere periodicity distance is found to be crucial to determine the light harvesting capability and subsequent PEC efficiency of the ultrathin film. This was evaluated based on micro-bent films of equal thickness, but with different plasma etching times from 10 to 40 min. The size of PS template spheres is reduced upon the increase of the etching time from 10 min to 40 min. The space between two neighboring spheres is inversely increased (Figures S3a-S3d), which shrinks the micro-space dimensions (Figures S4a-S4d) and thus shortens the effective optical path length and lowers the scattering effect in the micro-spaces. As inferred from **Figure 3a**, optical effects decrease with the increase of plasma etching time, especially in the range from 550 nm to 700 nm. After shortening the etching time the light coupling increases accompanied with a shifted and strong increase of absorption at the band gap. After etching for 10 and 20 min a new light absorbing structure located in front of the absorption

edge appears with peak positions at 650 nm after 10 min and 630 nm after 20 min etching time, respectively. It is worth mentioning that this additional absorption feature shifts to a higher wavelength and disappears again with increasing etching time. This observation is important to tailor the size dependent light absorption. Cyclic voltammetry (CV) has been further employed to evaluate the solar energy conversion efficiency of the micro-bent films as a function of increasing the etching time of PS template, as presented in Figure 3b. With increasing plasma etching time, the photocurrent initially increases to a maximum value of 0.59 mA cm^{-2} (20 min), and then decreases again to 0.1 mA cm^{-2} (40 min), proving that distance and diameter of the hollow hemispheres of the micro-structured films can be used to tune PEC performance. Modelling the behavior of this micro-structure the influence of hemisphere diameter was investigated (see below). As illustrated in Figure 3c, when keeping the dimensions of micro-spaces unchanged, the photocurrent steadily rises upon the film thickness until the film attains a thickness of 65 nm (Figure S5), however, further increase of the hematite film thickness results in the reduction of the photocurrent density. It is also anticipated that optimized PEC water splitting performance of the micro-bent ultrathin films can be achieved via angle dependent light enhanced absorption (Figure 3d), which is not found for planar hematite films of same thickness (see Figures S6).

For an improved understanding and prediction of optimal configurations, numerical 3D simulations of optical properties of the micro-bent films were performed. In accordance with the experiments, firstly different hemisphere sizes of radius r were investigated for equal pitch p (distance between the center of two spheres). The pitch was set to 480 nm and the radius to 235, 205, 175, 145 and 115 nm, respectively. **Figure 4a** exemplarily shows the spectral dependent absorption for the 235, 205 and 145 nm radius hollow hemisphere in comparison to the planar Fe_2O_3 film. Clearly, a strong increase in absorption can be observed which is most pronounced in the wavelength range above 500 nm. Above 600 nm wavelength, the absorption spectra of the hemisphere structures are dominated by multiple strong resonance

peaks due to coupled optical phenomena. As a function of hemisphere diameter the spectral position as well as the intensity of the peaks shift. A trend similar to the experimental observation shown in Figure 3a may be retraced, yet the resolution of individual resonances is not feasible in the experiment and only broad peaks can be observed in the long wavelength range in this case. Figure 4b reveals the light distribution in the hemisphere by showing the normalized electric field maps. An equivalent resonance – from the point of view of light distribution in the FTO substrate – was chosen for the three different radius 145, 205 and 235 nm and the electric field distribution is shown for the two polarization directions (yz- and zx-plane) where x, y and z are the directions in the hexagonal cell used for this calculation. The different field profiles in and perpendicular to the polarization direction (which was chosen to be the y-direction) can clearly be seen. Due to the hexagonal arrangement of the hemisphere a combination of both polarizations would not just mean averaging over the field distributions shown in Figure 4b but require considering calculations with light polarized in the x-direction. As it can be seen from the near-field pictures on the bottom row of Figure 4b, depending on the hemisphere size a different number of field maxima fit into the Fe_2O_3 film: 1, 3 and 5 for 145, 205 and 235 nm radius, starting from the left. The right picture also relates to the 235 nm radius structures, but for geometry closer to the experiment by considering a nanoarch rather than a hollow hemisphere (see Figures 1d, 1g and S7b). The exact wavelength of the chosen reference resonance position (in the FTO) slightly shifts. The light localization, i.e. the high electric field intensity, at the edges of the micro-arch is suppressed, but is yet more pronounced along the arch. Thus, an even more pronounced enhancement can be expected for an arch shaped micro/nano-structure.

The inset in the top left of Figure 4c (and enlarged in supporting information Figure S8) compares the absorption in Fe_2O_3 for the two cases of a 235 nm radius hollow micro-hemisphere of constant thickness and an arch (Figure 1d) with narrowing thickness in the cross section of the hollow hemisphere. Whilst on the first glance the absorption of the

narrowing arch type hollow hemisphere structure appears to be much lower, it needs to be taken into account that the volume of Fe_2O_3 is also much lower in this case. To address the changes in volume related to the different shapes, the short circuit current densities j_{SC} calculated from the absorption spectra were normalized to the Fe_2O_3 volume. Furthermore, the values were related to the performance of the planar Fe_2O_3 film, resulting in relative j_{SC}/Vol . This number is indeed significantly higher for the narrowing arch type hollow sphere than for the assumed hollow hemispheres with constant arch thickness – 1.29 compared to 0.89 – underlining the improved field localization in the arch as observed from the electric field pictures. The main part of Figure 4c summarizes the relative j_{SC}/Vol for various hollow micro-sphere radii and pitches. The right column relates to the case of constant pitch of 480 nm and different radii as discussed in Figure 4a. A clear trend towards increased relative absorption/current generation per Fe_2O_3 volume is observed with decreasing hollow hemisphere radius. An even better improvement may be expected for smaller hemisphere radius which means also smaller pitches, which could indeed be confirmed, compare the values on the diagonal of the plot. In this case, hemisphere diameter and pitch were reduced in the same way and the best performance was observed for the smallest pitch and radius investigated, namely 240 nm and 115 nm, respectively (10 nm were always added to the pitch to avoid point contacts between neighboring hemispheres in the simulations). An increase in j_{SC}/Vol of 3.5 times as compared to the planar Fe_2O_3 film was found for this micro-bent configuration.

Figure 4d depicts the calculated spectral dependent performance of the hollow hemisphere micro-structure with different radius and pitch corresponding to their diameter. As for the cases shown in Figure 4a a clearly superior absorption compared to the planar Fe_2O_3 film occurs. With decreasing hemisphere radius and pitch the resonances caused by coupled optical phenomena blue shift and become less pronounced for the smaller nanoarchs where less modes can fit in. The calculated curve for $(r, p) = (115, 240)$ nm in Figure 4d comes

closest to the absorption curves shown in Figure 3a for micro-bent films after 10 and 20 min etching time of the PS template, respectively. As discussed above a sharp increase of absorption occurs with a pre-peak at about 630 and 650 nm which is visible in the calculated curve as a hump at 660 nm. However, for the smallest hemispheres the enhancement is much more pronounced in the wavelength range from 500 - 600 nm and experiences the strongest amplification by the solar spectrum. Therefore, the array of hollow hemisphere microstructure performs best with hemispheres of radius $r = 115$ nm and is highly promising for further optimization of the experimental structures for example by lowering the hemisphere radius. Comparing the volume of the structured film per unit area to a flat film with a uniform thickness $d = 65$ nm the volume of the structured film is by a factor 2.8 larger. This means that the improved current density can partially be explained by the higher light absorption per unit area owing to the larger volume of the micro-bent film by arch formation. However, the higher volume cannot exclusively explain the improvement of relative current density improvement of factor of 4.5. The micro-bent also contribute by at least a factor of 1.6 to the observed improvement of current density which can be explained by the coupled optical light absorption. The calculations have shown that a lowering of the radius r of the hollow hemispheres to 115 nm should lead to a further improvement by a factor of 4.5 although here the light absorption is only improved by a factor of 2.1. Aside the consideration of current generated per absorber value, the extraction of the charge carriers is also important from the experimental point of view and may be improved for smaller hemisphere radius.

In summary, we have demonstrated in this communication a general approach to reshape the ultrathin film geometry to harvest more incident light for enhanced solar energy conversion, especially for light-induced water oxidation, which is an effective alternative for externally optical engineering of ultrathin solar fuel films. This geometry reconfiguration is not only leading to a higher light absorbing volume per unit area, but also to a complex enhanced light

coupling by photonic effects. The flexible manipulation of ultrathin films that introduces a controlled length scale periodicity in the microstructure could further optimize the film light harvesting and thus photocurrent generation. The numerical 3D simulations of optical properties of the micro-bent films indicates a clearly superior absorption compared to the planar Fe_2O_3 film, and the hollow hemisphere diameter strongly influences the PEC water splitting performance, which are in good agreement with our experimental results. It is thus anticipated that such strategy of geometrical reconfiguration is promising for developing photoelectrodes for efficient solar energy harvesting. Furthermore, the versatility of the present strategy combining self-assembly and magnetron sputtering allows for the construction of ultrathin films with desired compositions and architectures, for example, introducing an additional reflection layer beneath the micro-bent film to explore the light harvesting amplification by both, internal light resonance and external light scattering.

Experimental Section

Hematite thin film preparation: Fluorine-doped Tin Oxide (FTO) substrates were employed as transparent supports. Before deposition, all substrates were cleaned by sonication in acetone, ethanol, and finally water and dried in an N_2 gas flow afterwards. After that, a monolayer colloidal PS template with 500 nm sphere diameter was prepared on the FTO glass substrate by a self-assembly route. Typically, the as-purchased PS spheres from Alfa Aesar Company were diluted with an equal volume of ethanol, and then few drops PS suspension were first dropped onto one piece of cleaned normal microscopy glass substrate. After that, the glass substrate was slowly immersed in a beaker containing distilled water. Then, a monolayer of PS spheres formed on the surface of the water. Next, the monolayer of PS spheres on the water surface was picked up with one piece of FTO substrate and dried in air. Subsequently, an argon plasma etching process ranging from 10 to 40 min was used to reduce the size of PS spheres. Afterwards, $\alpha\text{-Fe}_2\text{O}_3$ films were deposited at room temperature by

radio frequency (RF) magnetron sputtering on top of the PS spheres using a pure hematite sputter target. During the deposition, the reaction chamber was maintained at $4 \cdot 10^{-6}$ Pa under a steady Ar gas flow of 8 sccm. The Fe_2O_3 sputter target (3 inch diameter, 99.95% purity) was pre-sputtered for five minutes before reactive sputtering was started. The distance between the sputter target and the substrate was 66 mm for all deposition. The deposition time was varied from 30 to 120 min. The purity of the Ar gas was 99.99%. After deposition the samples were annealed in air at 800 °C for 10 minutes to remove the PS template and to obtain the hollow semi-sphere array.

Film Characterization and Optical Measurements: The morphology of thin hematite films were characterized using a high-resolution scanning electron microscope (LEO 1530 from Zeiss). The crystal structure was determined by X-ray diffractometry (XRD) using a D8-Advanced Bruker diffractometer with a $\text{Cu-K}\alpha$ X-ray source in Bragg-Brentano geometry. Optical behavior of the layers was determined using a UV-Vis spectrometer (Lambda 950, Perkin-Elmer) equipped with an InGaAs detector (≤ 0.05 nm) in the UV-Vis range using a 150 mm diameter Ulbricht hemisphere. Spectrolon was used as standard for 100% reflectance. As radiation source a deuterium lamp (UV) and a wolfram lamp (Vis/IR) were applied, respectively.

Photoelectrochemical PEC Testing: Photocurrent measurements were performed to determine the solar photocurrent of the photoanodes in a three-electrode compartment (EG&G, 273A). 1 M KOH aqueous solution of pH 13.6, a Pt wire, and an Hg/HgO electrode were employed as electrolyte, counter electrode, and reference electrode, respectively. A tungsten halogen lamp (Xenophot) was used as light source. The lamp was adjusted to a light intensity of 40 mWcm^{-2} related to the wavelength range from 300 to 600 nm fitting to the light absorption of hematite. This intensity is close to the value of solar light in the related wavelength range corresponding to an intensity 30 mWcm^{-2} . However, we have to note that the spectral distribution of the light differs from AM1.5. All measurements were performed illuminating the films via the

electrolyte to investigate the hematite/electrolyte interface and via the transparent conductive oxide through a 0.32 cm^2 mask that defines the electrode area exposed to the electrolyte and the light. The potential of the hematite photoanodes was swept at a scan rate of 10 mV s^{-1} from cathodic to anodic potentials. The potential was converted to the reversible hydrogen electrode (RHE) potential. Incident-photon-to-current efficiency (IPCE) was measured using light from a 300 W xenon arc lamp (Oriel, model 6295) in combination with a grating monochromator (Acton SpectraPro 150i). A long-pass colored glass filter (Schott, 3 mm thick) was used to remove the second order of the diffracted light. The light intensity was measured as a function of wavelength with a calibrated photodiode (PD 300-UV, Ophir).

Optical Simulations: 3-dimensional optical simulations were performed using the software package Comsol Multiphysics [www.comsol.de]. A hexagonal unit cell with periodic boundary conditions was assumed in which a nanoarch made from Fe_2O_3 in a surrounding of air was centered. The nanoarch was represented by a hemispherical shell with a thickness of 65 nm and the area in between the nanoarchs was filled with a 65 nm thick layer of Fe_2O_3 as well. According to the experiment, the substrate was made from FTO on glass and perfectly matched layers (PML) completed the simulation structure on top and bottom (z-direction). Light was incident from the glass and polarized along the y-direction. Refractive index data for Fe_2O_3 were taken from [M. R. Querry. Optical constants, US Military Contractor Report CRDC-CR-85034 (1985) – via refractiveindex.info] and for FTO from [M. Schmid, PhD Thesis FU Berlin 2010]. The absorption in the Fe_2O_3 material was extracted from the simulations and converted into a short circuit current density by folding with the AM1.5 solar spectrum and integrating in the spectral range from 300 to 800 nm.

Supporting Information

Supporting Information is available from the Wiley Online Library or from the author.

Acknowledgements

L. C. Jia. acknowledges the financial support from the Fundamental Research Funds for the Central Universities (No.GK201702007). H. Q. Wang. acknowledges the financial support from the Fundamental Research Funds for the Central Universities (G2017KY0002), Natural Science Foundation of Shaanxi Province (2017JM5028), the National Natural Science Foundation of China (No. 51672225), and the 1000 Youth Talent Program of China. This work was supported by the German Research Association (DFG) in the Priority Program SPP1613 under contract # FI 1524/3-1, entitled “Nanostructured transition metal oxide electrodes for the light-induced water splitting – a combinatorial approach”. Technical support performing sputtering experiments by Karsten Harbauer is gratefully acknowledged.

Received: ((will be filled in by the editorial staff))

Revised: ((will be filled in by the editorial staff))

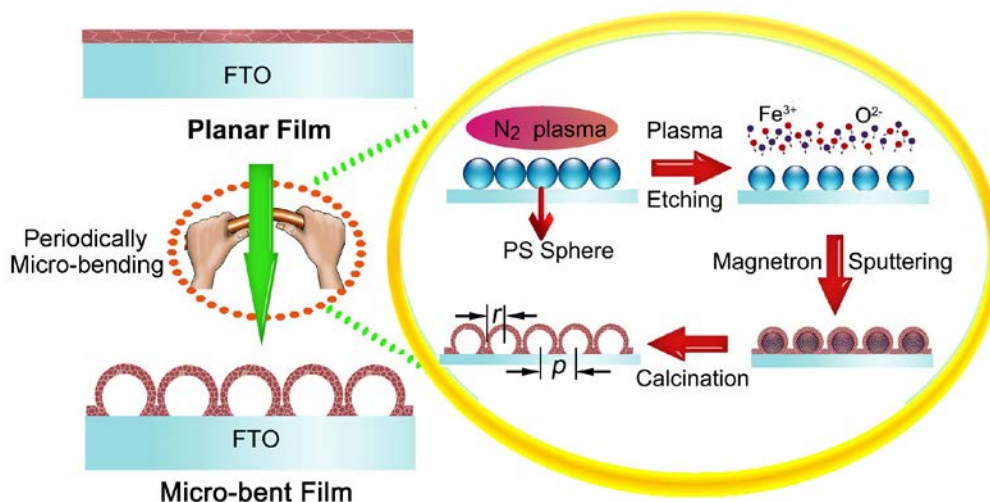
Published online: ((will be filled in by the editorial staff))

References

- [1] a) K. Sivula and R. van de Krol, *Nat. Rev. Mater.* **2016**, *1*, 15010; b) C. R. Jiang, S. J. A. Moniz, A. Q. Wang, T. Zhang, J. W. Tang, *Chem. Soc. Rev.* **2017**, *46*, 4645; c) T. Hisatomi, J. Kubota, K. Domen, *Chem. Soc. Rev.* **2014**, *43*, 7520; d) X. Li, J. G. Yu, J. X. Low, Y. P. Fang, J. Xiao, X. B. Chen, *J. Mater. Chem. A* **2015**, *3*, 2485.
- [2] a) H. Dotan, O. Kfir, E. Sharlin, O. Blank, M. Gross, I. Dumchin, G. Ankonina, A. Rothschild, *Nat. Mater.* **2013**, *12*, 158; b) S.-Fung Leung, Q. P. Zhang, M. M. Tavakoli, J. He, X. L. Mo, Z. Y. Fan, *small* **2016**, *12*, 2536; c) M. Burrelli, F. Pratesi, F. Riboli, D. S. Wiersma, *Adv. Optical Mater.* **2015**, *3*, 722.
- [3] a) M. Barroso, S. R. Pendlebury, A. J. Cowan, J. R. Durrant, *Chem. Science* **2013**, *4*, 2724; b) J.-W. Jang, D. Friedrich, S. Müller, M. Lamers, H. Hempel, S. Lardhi, Z. Cao, M. Harb, L. Cavallo, R. Heller, R. Eichberger, R. van de Krol, F. F. Abdi., *Adv. Energy Mater.* **2017**, *1701536*, 1; c) M. Z. Liu, J. L. Lyons, D.H. Yan, M. S. Hybertsen, *Adv. Funct. Mater.* **2016**, *26*, 219.
- [4] a) H. M. Chen, C. K. Chen, R.-S. Liu, L. Zhang, J. Zhang, D. P. Wilkinson, *Chem. Soc. Rev.* **2012**, *41*, 5654; b) I. S. Cho, H. S. Han, M. Logar, J. Park, X. L. Zheng, *Adv. Energy Mater.* **2016**, *6*, 1501840; c) Q. Liu, F. R. Cao, F. L. Wu, H. Lu, L. Li, *Adv. Mater. Interfaces* **2016**, *3*, 1600256.

- [5] Y. Lin, G. Yuan, S. Sheehan, S. Zhou, D. Wang, *Energy Environ. Sci.* **2011**, *4*, 4862.
- [6] a) W. Q. Wu, H. L. Feng, H. S. Rao, Y. F. Xu, D. B. Kuang, C. Y. Su, *Nat. Commun.* **2014**, *5*, 3968; b) C. Cheng, W. Ren, H. Zhang, *Nano Energy* **2014**, *5*, 132; c) J. Shi, Y. Hara, C. Sun, M. A. Anderson, X. Wang, *Nano Letters* **2011**, *11*, 3413.
- [7] a) J. S. Kang, Y. S. Noh, J. Kim, H. Choi, T. H. Jeon, D. Ahn, J.-Y. Kim, S.-H. Yu, H. Park, J.-H. Yum, W. Y. Choi, D. C. Dunand, H. Choe, Y.-E. Sung, *Angew. Chem. Int. Ed.* **2017**, *56*, 6583; b) A. Sivanantham, P. Ganesan, S. Shanmugam, *Adv. Funct. Mater.* **2016**, *26*, 4661; c) C. L. Zhang, M. F. Shaon, F. Y. Ning, S. M. Xu, Z. H. Li, M. Wein, D. G. Evans, X. Duan, *Nano Energy* **2015**, *12*, 231.
- [8] a) X. Shi, K. Zhang, K. Shin, J. H. Moon, T. W. Lee, J. H. Park, *Phys. Chem. Chem. Phys.* **2013**, *15*, 11717; b) L. Zhang, D. Bahnemann, *ChemSusChem* **2013**, *6*, 283; c) L. N. Quan, Y. H. Jang, K. A. Stoerzinger, K. J. May, Y. J. Jang, S. T. Kochuveedu, Y. S.-Horn, D. H. Kim, *Phys. Chem. Chem. Phys.* **2014**, *16*, 9023; d) F. Sordello, V. Maurino, C. Minero, *J. Mater. Chem. A* **2011**, *21*, 19144.
- [9] a) J. Yu, Q. Q. Li, Y. Li, C. Y. Xu, L. Zhen, V. P. Dravid, J. S. Wu, *Adv. Funct. Mater.* **2016**, *26*, 7644; b) Y. Yang, Q. Jin, D. Mao, J. Qi, Y. Z. Wei, R. B. Yu, A. Li, S. Z. Li, H. J. Zhao, Y. W. Ma, L. H. Wang, W. P. Hu, D. Wang, *Adv. Mater.* **2017**, *29*, 1604795;
- [10] a) G. Yun, M. Balamurugan, H.-S. Kim, K.-S. Ahn, S. H. Kang, *J. Phys. Chem. C* **2016**, *120*, 5906; b) X. Li Zheng, J. P. Song, T. Ling, Z. P. Hu, P.-F. Yin, K. Davey, X.-W. Du, S.-Z. Qiao, *Adv. Mater.* **2016**, *28*, 4935.
- [11] X. Shi, K. Zhang, J. H. Park, *Int. J. Hydrogen Energy* **2013**, *38*, 12725.
- [12] L. Zhang, E. Reisner, J. J. Baumberg, *Energy Environ. Sci.* **2014**, *7*, 1402.
- [13] K. Kim, P. Thiyagarajan, H. J. Ahn, S. I. Kim, J. H. Jang, *Nanoscale* **2013**, *5*, 6254.
- [14] S. J. Kim, I. Thomann, J. Park, J. H. Kang, A. P. Vasudev, M. L. Brongersma, *Nano Letters* **2014**, *14*, 1446.

- [15] J. Li, S. K. Cushing, P. Zheng, F. Meng, D. Chu, N. Wu, *Nat. Commun.* **2013**, *4*, 2651.
- [16] Y. Lu, H. Yu, S. Chen, X. Quan, H. Zhao, *Environ. Sci. Technol.* **2012**, *46*, 1724.
- [17] J. Liu, G. Liu, M. Li, W. Shen, Z. Liu, J. Wang, J. Zhao, L. Jiang, Y. Song, *Energy Environ. Sci.* **2010**, *3*, 1503.
- [18] K. X. Wang, Z. Yu, V. Liu, M. L. Brongersma, T. F. Jaramillo, S. Fan, *ACS Photonics* **2014**, *1*, 235.
- [19] F. Boudoire, R. Toth, J. Heier, A. Braun, E. C. Constable, *Energy Environ. Sci.* **2014**, *7*, 2680.
- [20] Y. Qiu, S.-F. Leung, Q. Zhang, B. Hua, Q. Lin, Z. Wei, K.-H. Tsui, Y. Zhang, S. Yang, Z. Fan, *Nano Letters* **2014**, *14*, 2123.
- [21] a) M. Valenti, E. Kontoleta, I. A. Digdaya, M. P. Jonsson, G. Biskos, A. S.-Ott, W. A. Smith, *ChemNanoMat* **2016**, *2*, 739; b) L. Wang, H. Y. Hu, N. T. Nguyen, Y. J. Zhang, P. Schmuki, Y. P. Bi, *Nano Energy* **2017**, *35*, 171.
- [22] M. P. Dare-Edwards, J. P. Goodnough, A. Hamnett and P. R. Trevellick, *J. Chem. Soc., Faraday Trans.* **1983**, *79*, 20271.
- [23] J. H. Kennedy and K. W. Frese, *J. Electrochem. Soc.*, **1978**, *125*, 709.
- [24] Y. Yin, Y. Lu, B. Gates, Y. Xia, *J. Am. Chem. Soc.* **2001**, *123*, 8718.
- [25] C. W. Wang, S. Yang, H. B. Jiang, H. G. Yang. *Chem. Eur. J.* **2015**, *21*, 18024
- [26] J. Moir, N. Soheilnia, K. Liao, P. O'Brien, Y. Tian, K. S. Burch, G. A. Ozin, *ChemSusChem* **2015**, *8*, 1557.
- [27] S. S. Fratoni, S. P. Perone, *Anal. Chem.* **1976**, *48*, 287.
- [28] F. Le Formal, K. Sivula, M. Grätzel, *J. Phys. Chem. C* **2012**, *116*, 26707.
- [29] A. Hagfeldt, H. Lindström, S. Södergren, S.-E. Lindquist, *J. Electroanal. Chem.* **1995**, *381*, 39.
- [30] L. M. Peter, *Chem. Rev.* **1990**, *90*, 753.



Scheme 1. Schematic illustration of the geometry reconfiguration of the planar $\alpha\text{-Fe}_2\text{O}_3$ film via periodically micro-bending to generate the arrays of hollow hemispheres with radius r , separated by the pitch p , composed of hematite nano-grains. This film architecture generates compared to a flat film a supplementary photonic structure for optical management of the incident light.

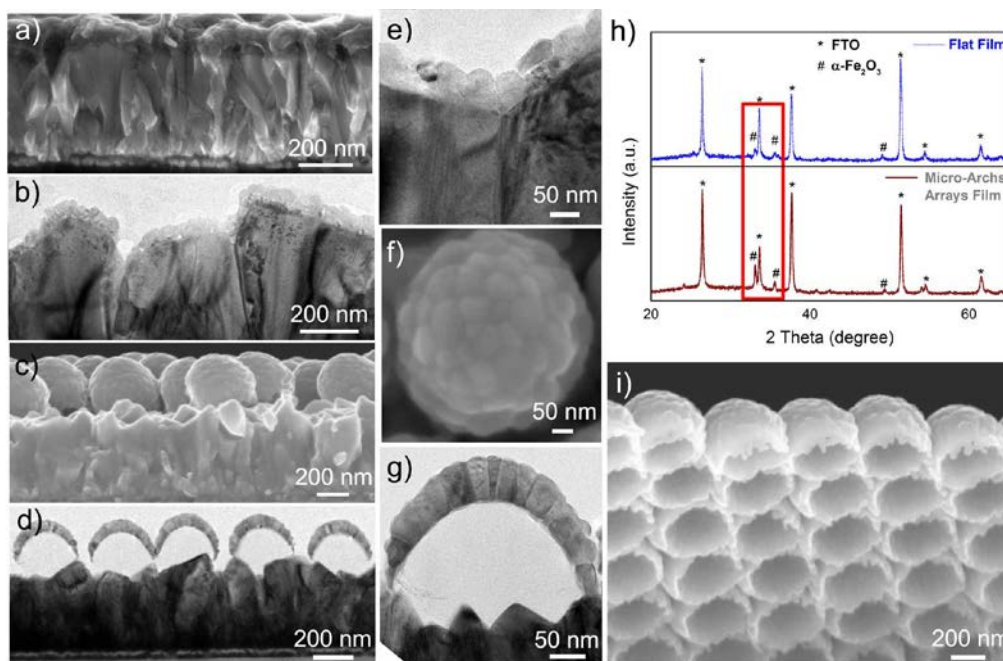


Figure 1. a-b) Cross-section SEM and TEM images of a planar hematite film deposited on FTO; c-d) Cross-section SEM and TEM images of the micro-bent film deposited on an FTO substrate (plasma etching of PS spheres 20min, sputter deposition 60min); e and g) Magnified cross-section TEM images of the planar film section and a thin oxide film after structuring; the arch-type structure represents a cross section of a micro arch the archola-type structure of which is shown in fig. 1.f., h) comparison of the XRD patterns of the planar hematite film and a film consisting of micro-bent section appearing as hollow microspheres; i) the bottom view of the micro-bent film after peeling off from a glass substrate.

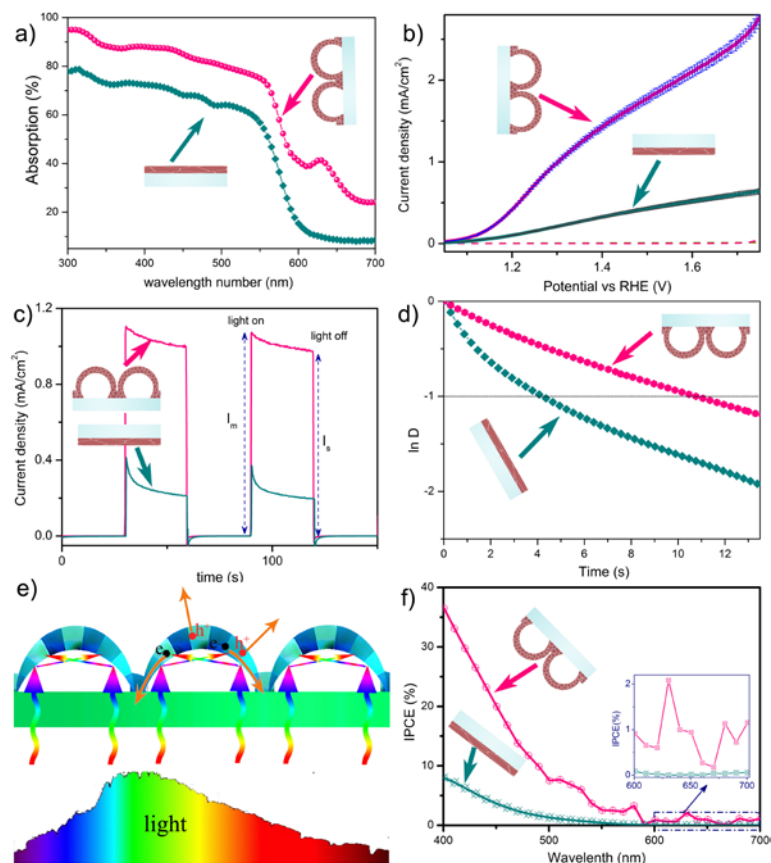


Figure 2. a) Ultraviolet-visible absorption spectra, b) Current densities vs. voltage curves, c) Transient photocurrent decay, d) Transient decay time and f) IPCE spectra of a film with micro-bent film architecture (plasma etching of the PS template 20min, deposition time from the hematite target 60min) versus a planar film geometry deposited on FTO (deposition time 60min). e) Schematic illustration of conversion efficiency enhancement by multi-light scattering within the micro-arch, hollow sphere array structure.

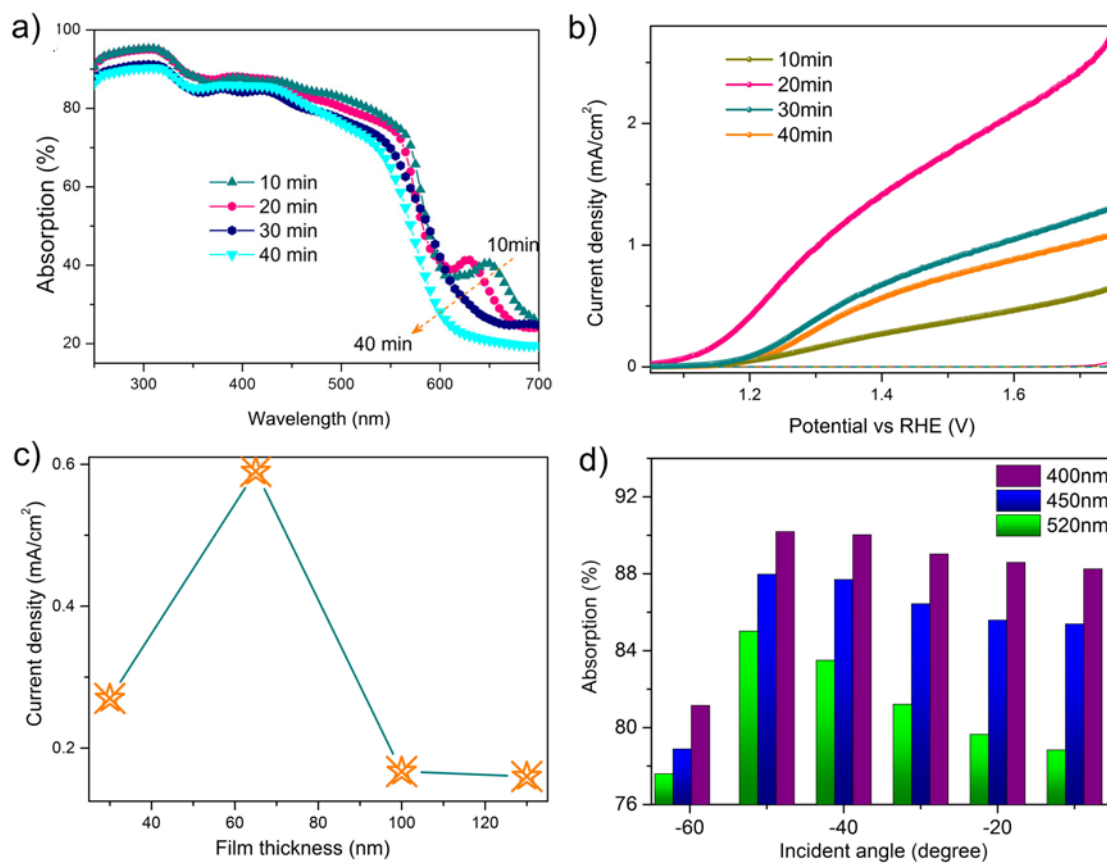


Figure 3. a) I-V curves (in the dark and under illumination), and b) ultraviolet-visible absorption spectra of micro-bent films treated by plasma etching with different time period; c) Photocurrent densities of the micro-bent film architecture (20 min plasma etching) as a function of film thickness at 1.23 V_{RHE} ; d) incident angle dependent variation of optical absorption behaviors for the micro-bent film (20 min plasma etching).

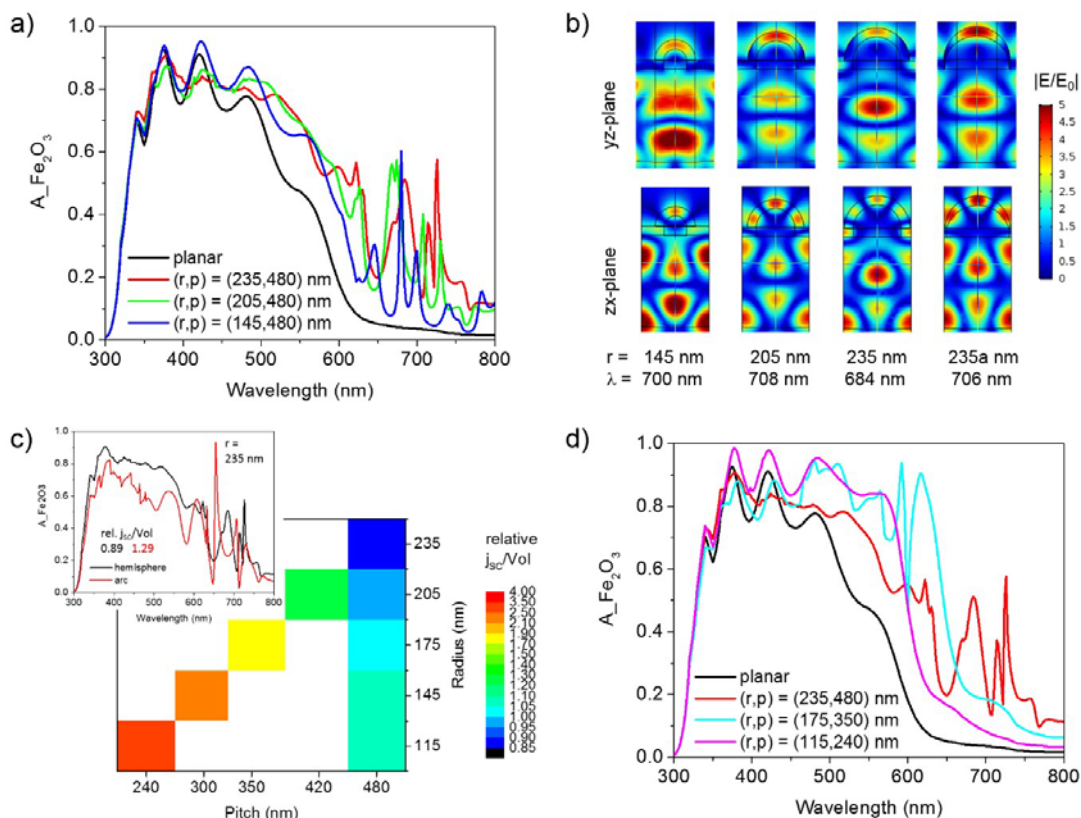
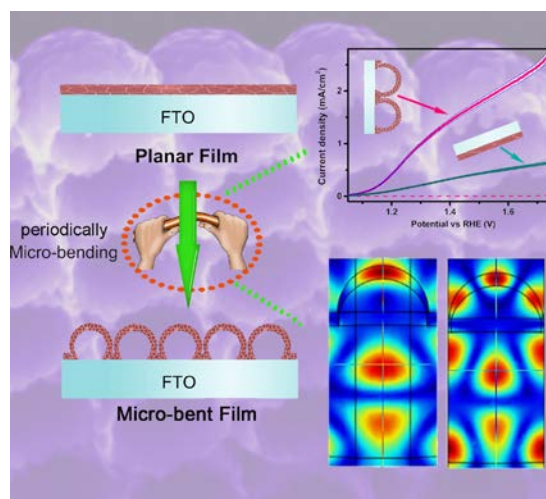


Figure 4. Optical simulation of nanoarch structures: a) absorption in $\alpha\text{-Fe}_2\text{O}_3$ for hexagonal nanoarch arrangements with 480 nm pitch and radii of 235, 205 and 145 nm as compared to planar reference, b) normalized electric field distributions in the two polarization directions for the nanoarch configurations shown in a) and for a radius 235 nm arc (235a nm), c) comparison of absorption in $\alpha\text{-Fe}_2\text{O}_3$ for the $r = 235$ nm hemispherical nanoarch and the corresponding arc (top left inset) and current density j_{sc} originating from absorption normalized to $\alpha\text{-Fe}_2\text{O}_3$ volume and planar reference for different radii and pitches (main figure), d) absorption in Fe_2O_3 for nanarchs with various radii and corresponding pitches to maintain close packing.

The geometry reconfiguration from Planar to periodically micro-bent film is not only leading to a higher light absorbing volume per unit area, but also to a complex enhanced light coupling by photonic effects, which has been verified to greatly benefit the enhancement of PEC solar water splitting performance.

L. C. Jia*, H. Q. Wang*, P. Bogdanoff, M. Schmid, U. Bloeck, S. Fiechter,

Reconfiguration of Solar Fuel Ultrathin Films via Periodically Micro-bending for Efficient Photo-electrochemical Water Splitting



Supporting Information

Reconfiguration of Solar Fuel Ultrathin Films via Periodically Micro-bending for Efficient Photo-electrochemical Water Splitting

*Lichao Jia**, *Hongqiang Wang**, *Peter Bogdanoff*, *Martina Schmid*, *Ulrike Bloeck*, and *Sebastian Fiechter*

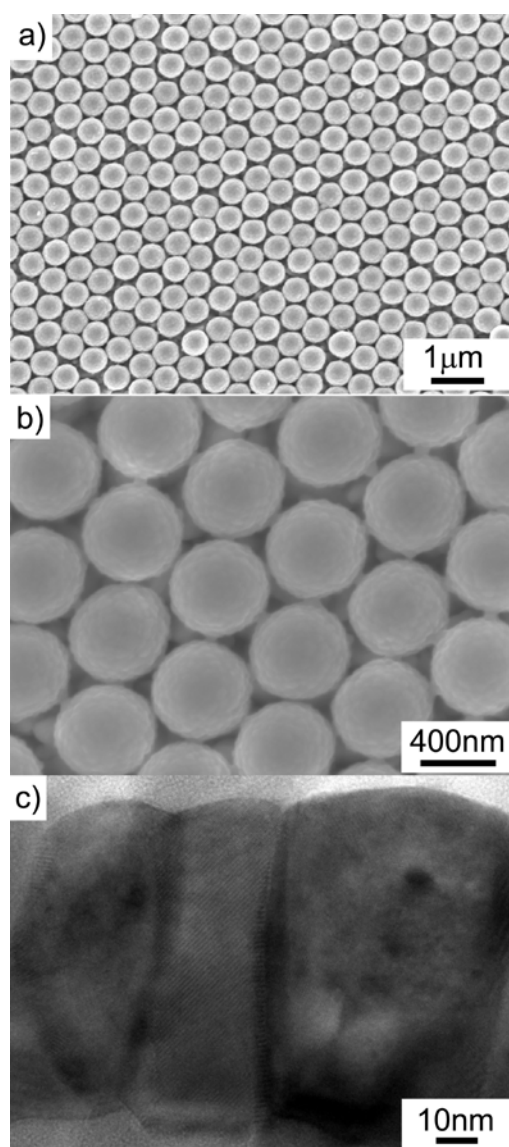


Figure S1 (a, b) FESEM top view images and (c) HRTEM cross section image of the hematite micro-bent film (plasma etching time 20min, deposited 60min). In (b) necking between the particles is visible.

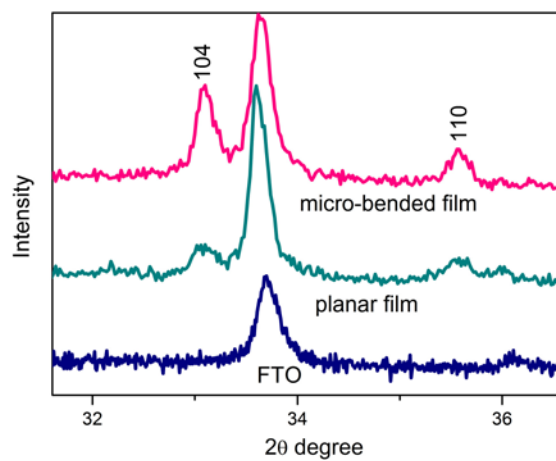


Figure S2. Enlarged XRD patterns of the planar film and Micro-bent film architecture shown in Figures 1a and 1c, respectively.

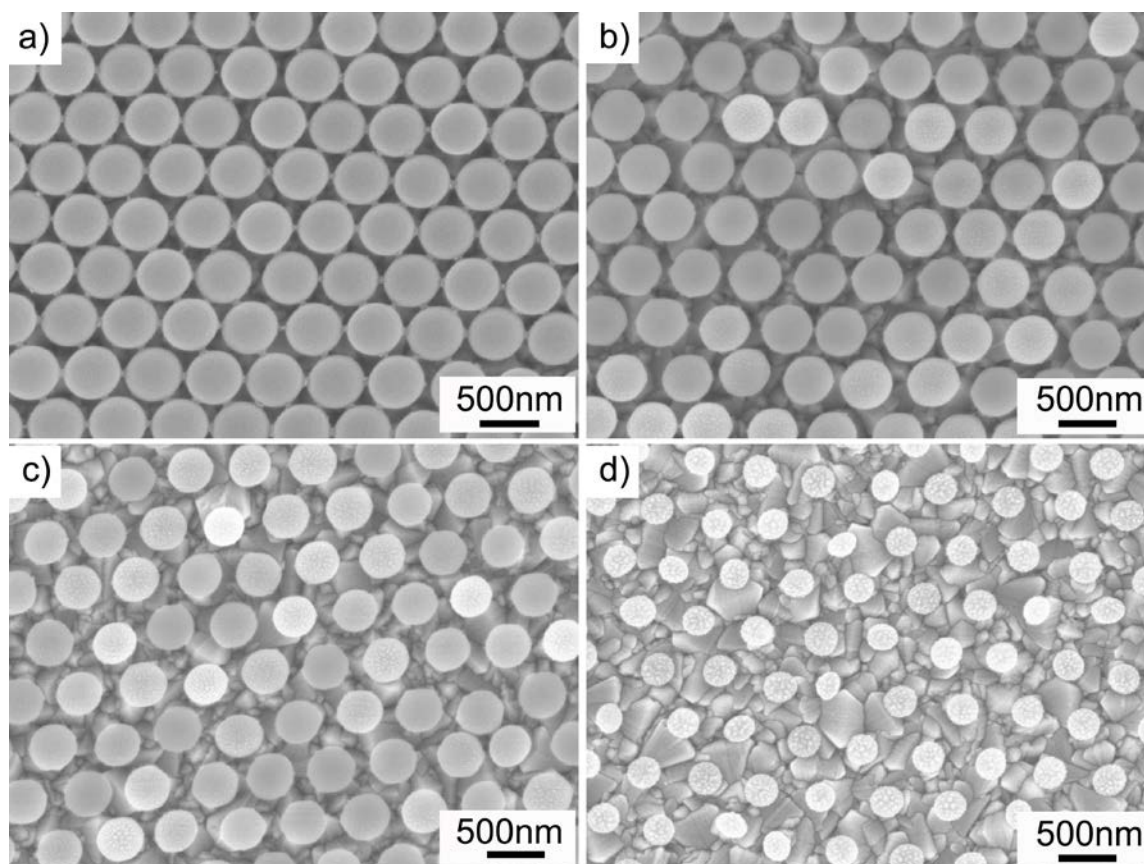


Figure S3 FESEM top view images of PS template upon plasma etching with different time period: (a) 10min, (b) 20min, (c) 30min and (d) 40min.

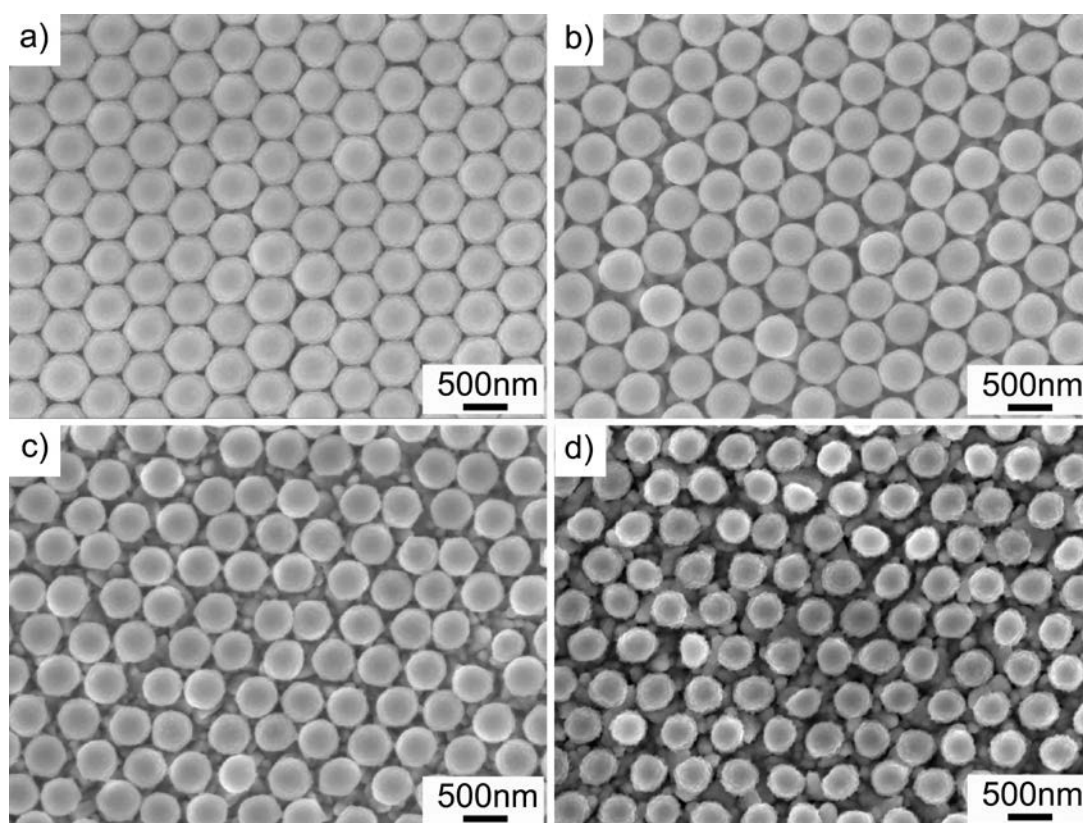


Figure S4. FESEM top view images of α - Fe_2O_3 Micro-bent film architecture deposited on PSs template treated with plasma etching: (a) 10min, (b) 20min, (c) 30min and (d) 40min.

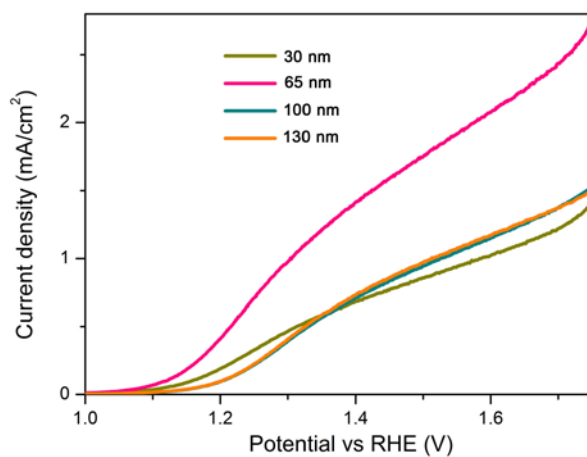


Figure S5. I-V curves of Micro-bent film architecture prepared by sputtering for different deposition time (PSs template treated by 20 min plasma etching).

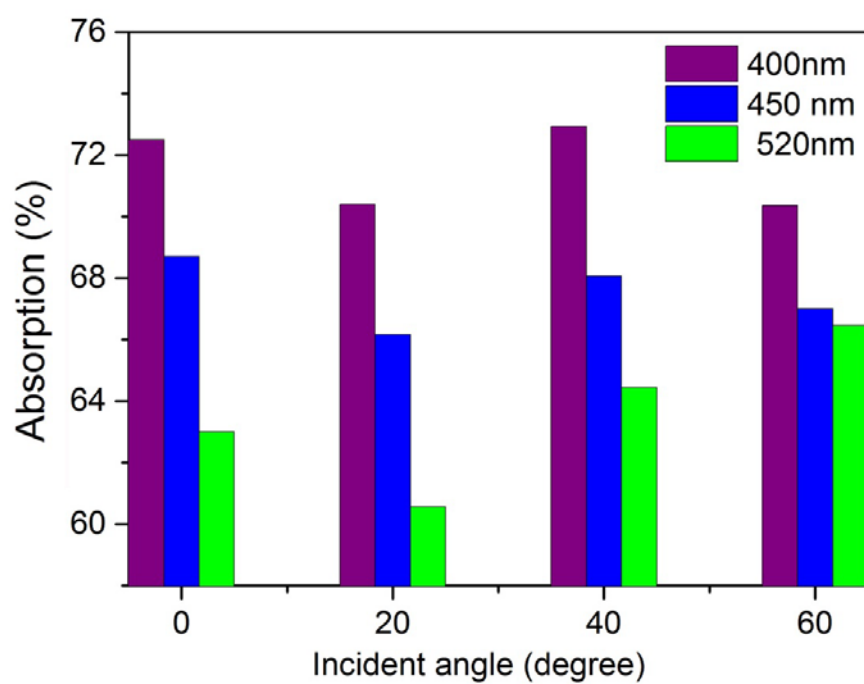
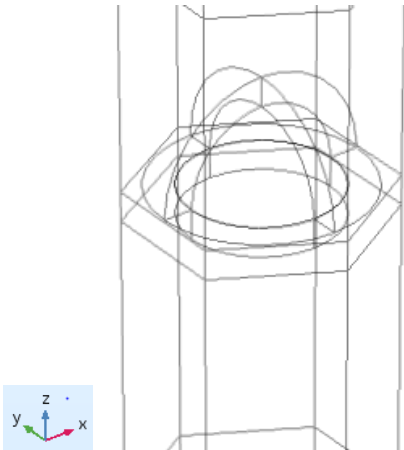
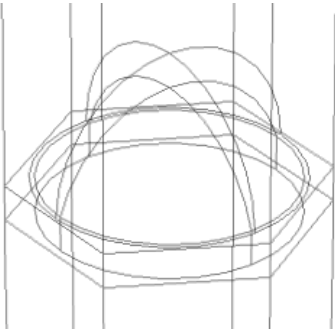


Figure S6. Absorption variation of the hematite planar film upon different incident angles.

 <p>A 3D schematic diagram of a hexagonal cell structure. The cell is a hexagonal prism. Inside, there is a complex, multi-layered arch structure. A small inset in the bottom left shows a 3D coordinate system with x, y, and z axes.</p>	 <p>A 3D schematic diagram of a hexagonal cell structure, similar to (a). The arch structure inside is more complex and appears to have a thickness that varies across its length, tapering towards the substrate.</p>
<p>Figure S7. Simulated structures using a hexagonal cell with an inscribed arch of constant thickness d (a) and an inscribed arch with a continuously reduced arc thickness d toward the substrate (b)</p>	
<p>Optical data used for the calculations: top air $(n,k) = (1,0)$ hemisphere shell Fe_2O_3 (n,k) from [34], thickness of shell or apex of arch: 65 nm inner space air: $(n,k) = (1,0)$ FTO layer (n,k) from [35], thickness: 650 nm glass substrate: $(n,k) = (1.5,0)$</p>	

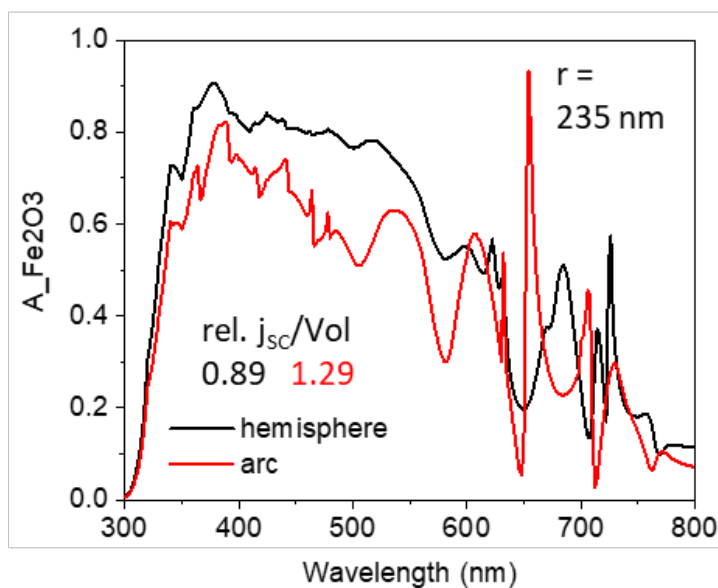


Figure S8. Comparison of the hollow hemisphere of arc thickness d (radius $r = 235$ nm, pitch $p = 480$ nm). Black curve: Absorption behaviour of arch of constant thickness $d = 65$ nm; red curve: absorption behaviour of an arch of a continuously reduced arc thickness toward the substrate with an thickness of $d = 65$ nm in the apex of the arch.